Chapter 6

Acceleration: Recirculating Linear Accelerator

Acceleration of a muon beam is a challenging task because of its large phase space and short lifetime. In the design concept presented here, acceleration starts after ionization cooling at 210 MeV/c and proceeds to 20 GeV, where the beam is injected into a Neutrino Factory storage ring. The key technical issues, beyond the basic physics parameters of Table 6.1, are:

- choice of acceleration technology (superconducting versus normal conducting cavities) and, related to it, rf frequency choice
- choice of acceleration scheme
- capture, acceleration, transport and preservation of a large-phase-space muon beam
- accelerator performance issues, such as potential collective effects (*e.g.*, cumulative beam breakup) resulting from the high peak current.

To minimize muon decay, the highest possible accelerating gradient is required; that is the main driver for the proposed scheme. The muon accelerator driver consists of a 2.87 GeV linac and a four-pass recirculating linear accelerator, as shown in Fig. 6.1.

Very large transverse and longitudinal accelerator acceptances drive the design to low rf frequency. If we were to use normal-conducting rf (NCRF) cavities, the required gradients would be of the order of 15 MV/m, which, in turn, demands extremely high peak power rf sources. Superconducting rf (SCRF) cavities are a much more attractive solution. RF power can then be delivered to the cavities over an extended time, and thus

Table 6.1: Main parameters of the muon accelerator driver.

Injection momentum (MeV/c)/Kinetic energy (MeV)	210/129.4
Final energy (GeV)	20
Initial normalized acceptance (mm-rad)	15
rms normalized emittance (mm-rad)	2.4
Initial longitudinal acceptance, $\Delta p L_b/m_\mu$ (mm)	170
momentum spread, $\Delta p/p$	± 0.21
bunch length, L_b (mm)	± 407
rms energy spread	0.084
rms bunch length (mm)	163
Number of bunches per pulse	67
Number of particles per bunch/per pulse	$4.4 \times 10^{10}/3 \times 10^{12}$
Bunch frequency/accelerating frequency (MHz)	201.25/201.25
Time structure of muon beam	6 pulses at 50 Hz; 2.5 Hz repetition rate
Average beam power (kW)	150

the rf source peak power can be reduced. Another important advantage of SCRF cavities is that their design is not limited by a requirement of low shunt impedance, and therefore their aperture can be significantly larger then would be practical for NCRF cavities. Taking into account the required longitudinal and transverse acceptances, and that the beam is already bunched at 201.25 MHz at the source (ionization cooling), a 201.25 MHz rf frequency has been chosen for both the linear accelerator and the recirculator. This choice provides adequate stored energy to accelerate multiple passes of a single-pulse bunch train without the need to refill the extracted energy between turns.

The short muon lifetime essentially excludes use of a conventional circular accelerator, and demands either a high-gradient conventional or recirculating linac (FFAG rings could be also considered). While recirculation provides significant cost savings over a single linac, it cannot be utilized at low energy for two reasons. First, at low energy the beam is not sufficiently relativistic and will therefore slip in phase on subsequent passes, thus significantly reducing acceleration efficiency. Second, there are major difficulties associated with injection of a beam with the large emittance and energy spread characteristic of a muon source. Beam pre-acceleration in a linear accelerator to about 2.5 GeV makes the beam sufficiently relativistic, and adiabatically decreases the phase-space volume, so that further acceleration in recirculating linacs is possible.

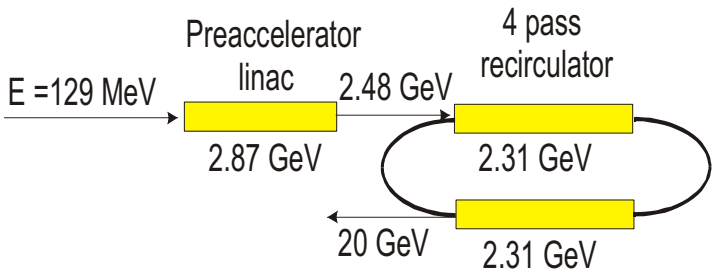

Figure 6.1: Layout of the muon accelerator driver.

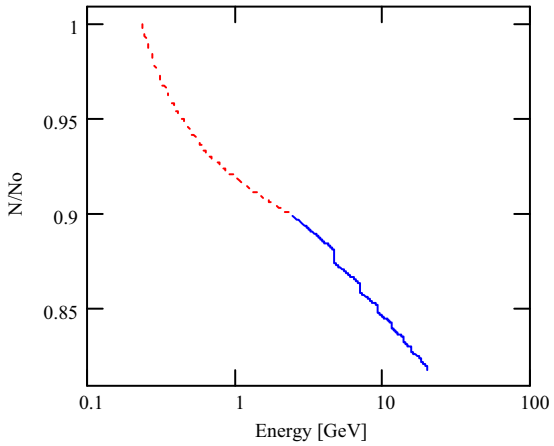

Figure 6.2: Decay of muons in the course of acceleration. The dotted line is the decay in the linac, and the solid line is the decay in the recirculator. Vertical drops correspond to the beam transport in arcs.

Cost considerations favor multiple passes per stage, but practical experience commissioning and operating recirculating linacs dictates prudence. Experience at Jefferson Lab suggests that for a given large initial emittance and energy spread, a ratio of final-to-injected energy below 10-to-1 is prudent, and the number of passes should be limited to about five. We therefore propose a machine architecture (see Fig. 6.1) featuring a 0.13-to-2.48 GeV straight "preaccelerator" linac, followed by a 2.48-to-20 GeV four-pass recirculating linac (RLA). Figure 6.2 shows the loss of muons during the course of acceleration. While the RLA gives a significant contribution, the major loss fraction comes from the linac. Note that the arcs (vertical drops in Fig. 6.2) do not contribute much to the decay, which justifies the choice of normal conducting bends, and triplet focusing discussed below.

Table 6.2: Main parameters of linear accelerator.

Injection momentum (MeV/c)/Kinetic energy (MeV)	210/129.4
Final momentum (MeV/c)/Kinetic energy (MeV)	2583/2480
Total linac length (m)	433
Acceptance: initial/final (no emittance dilution) (mm-rad)	7.5/0.62
Momentum spread: initial/final	$\pm$0.21/$\pm$0.075
Total bunch length: initial/final (mm)	814/190
(deg.)	197/46
Total installed accelerating voltage (GeV)	2.87

6.1 Linear Accelerator

6.1.1 Matching

It is important to provide a section that matches the beam ellipse from what it is in the cooling section to what it is in this linac. That matching section is described in Section 5.5. The lattice not only matches the beam ellipses, it accelerates by a small amount, approximately 59 MeV. Using the phase graph in Fig. 6.11, we compute that approximately the first 38 m of the linac described in this Chapter is no longer required, that is, only the last 4 short cryomodules are needed. In this Chapter, however, we ignore the acceleration in the matching section, and assume that we start accelerating at a momentum of 210 MeV/c.

6.1.2 Linac General Parameters and Lattice Period Layout

The requirement for a large acceptance of the accelerator necessitates a large aperture and tight focusing at its upstream end. Considering the large aperture, the tight space, the moderate beam energy and the need for strong focusing in both planes, solenoidal focusing is superior to triplet focusing, and has been chosen for the entire linac. To achieve a manageable beam size in the initial portion of the linac, short focusing cells are used for the first 11 cryomodules. As the beam size adiabatically damps during acceleration, intermediate-length cryomodules can be used and finally, when the energy reaches 0.75 GeV long (standard) cryomodules are utilized for the remainder of the linac. In comparison with the standard 13 m cryomodules, the short and intermediate-length cryomodules have increased aperture and, consequently, reduced accelerating gradient. The main parameters of the linac and its three cryomodule types are presented in Tables 6.2 and

Table 6.3: Parameters for the linear accelerator cryomodules.

	Short	Intermediate	Long
Number of periods	11	16	19
Total length of one period (m)	5	8	13
Number of cavities per period	1	2	4
Number of cells per cavity	2	2	2
Number of couplers per cavity	2	2	2
Cavity accelerating gradients (MV/m)	15	15	17
Real-estate gradient (MV/m)	4.47	5.59	7.79
Aperture in cavities ($2a$) (mm)	460	460	300
Aperture in solenoids ($2a$) (mm)	460	460	360
Solenoid length (m)	1	1	1.5
Solenoid maximum field (T)	2.1	2.1	4.2

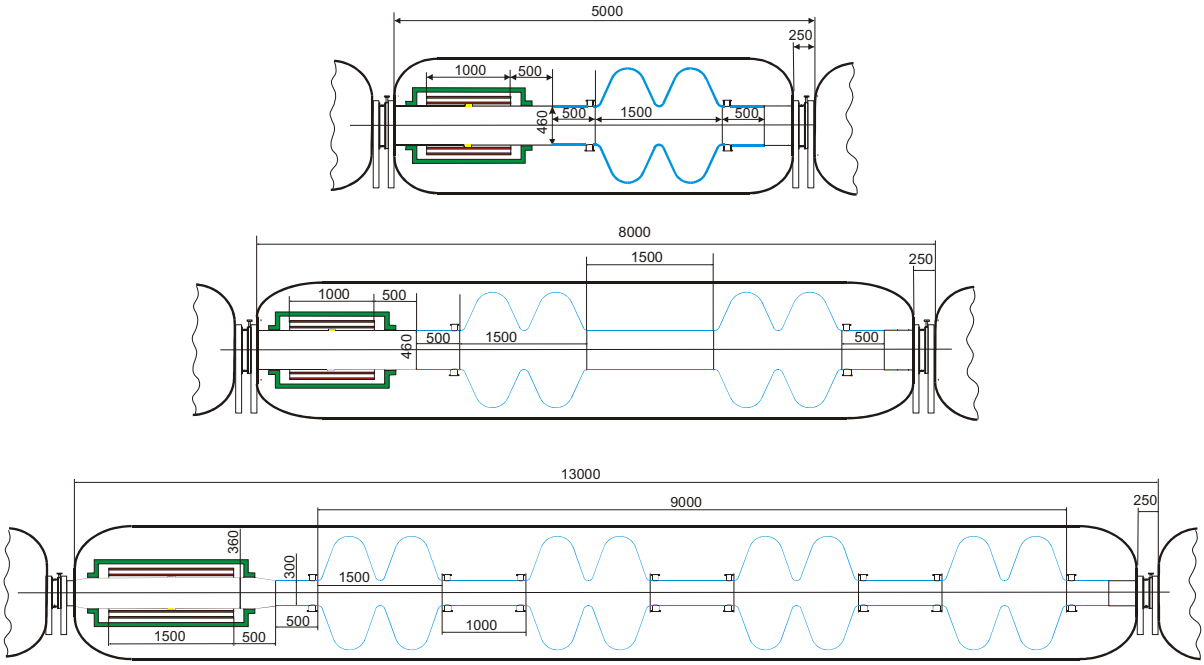

Figure 6.3: Layouts of short (top), intermediate (middle) and long (bottom) cryomodules. Blue lines are the SC walls of the cavities. Solenoid coils are indicated in red, and BPMs in yellow.

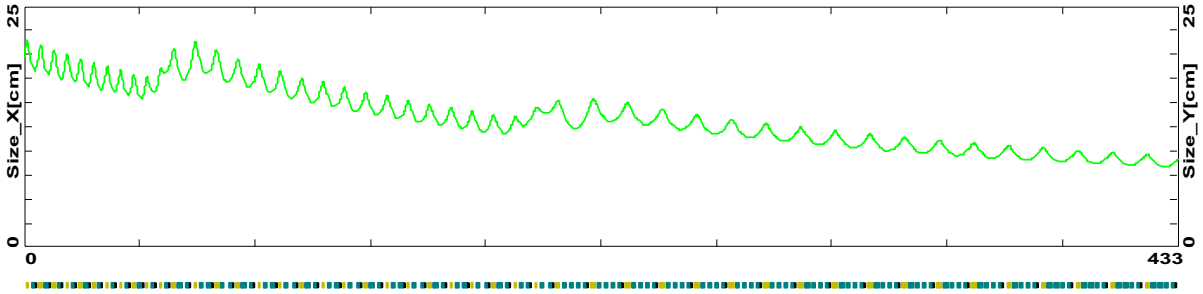

Figure 6.4: Beam envelopes of the entire beam (2.5σ) along the linear accelerator.

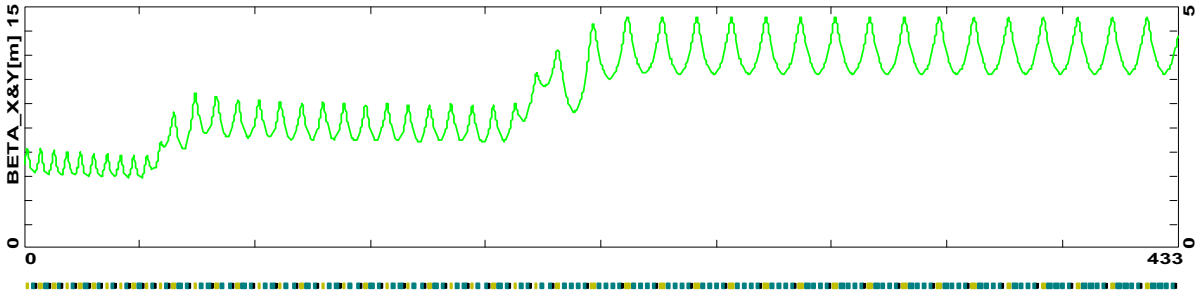

Figure 6.5: Beta functions along the linear accelerator. The beta functions are computed in the frame that rotates with angular frequency $\omega = eB_s/2pc$, so that the beam motion is decoupled.

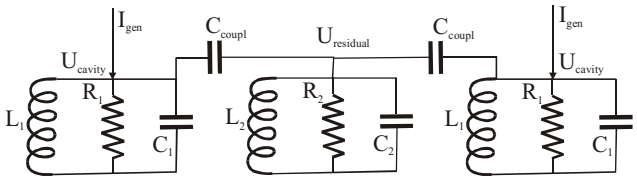

Figure 6.6: Electrical circuit model for calculation of cavity coupling.

6.3. Figure 6.3 depicts the layouts of short, intermediate-length and long cryomodules. Figures 6.4 and 6.5 present the beam envelope and beta-function along the linac.

The layout of cryomodules and the arrangement of SC cavities are determined by the requirement to keep power through the fundamental coupler at an acceptable level and to have cavities sufficiently decoupled. The coupler power limitation (below 0.5 MW) requires 1 coupler per cell, so there is a coupler at each end of the two-cell cavity.

The coupling coefficient determined as $\delta = C_3/C_1$ (see Fig. 6.6), should be sufficiently

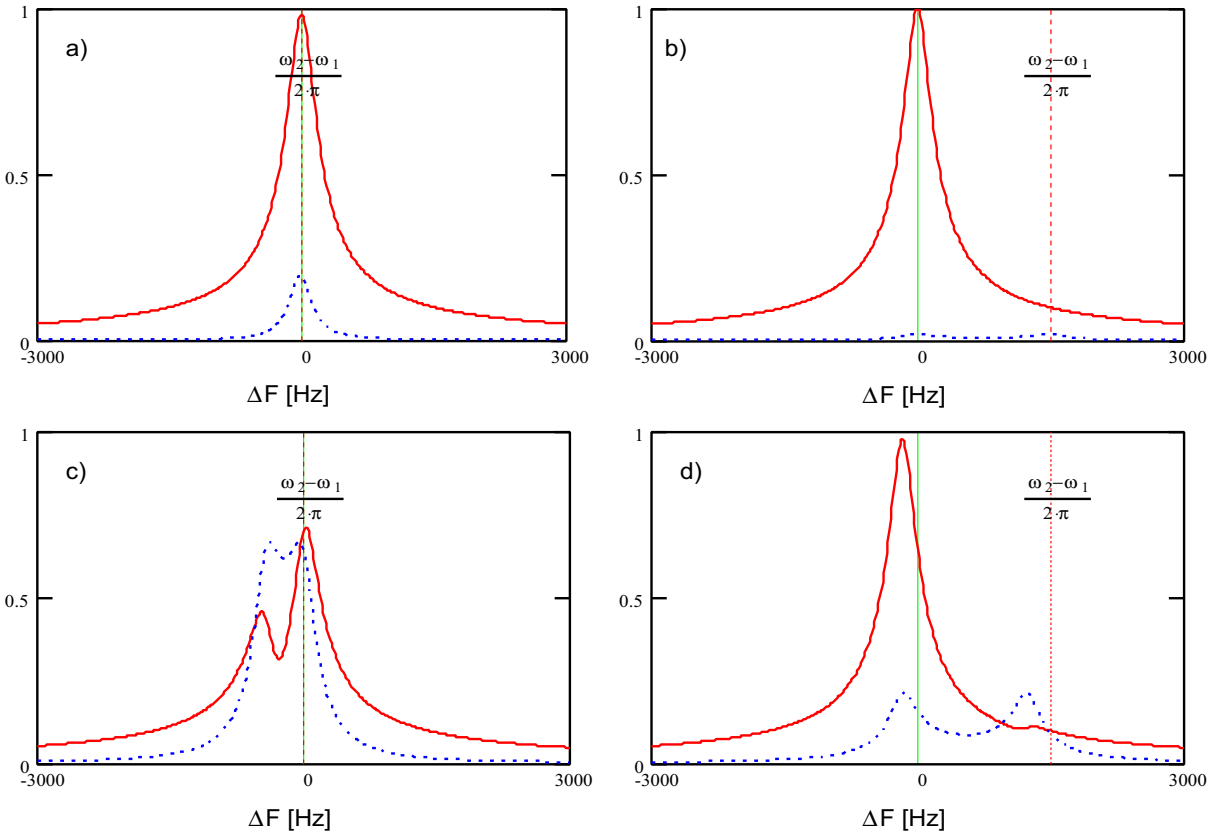

Figure 6.7: Dependence of cavity voltage on frequency. Solid lines: voltage for normally powered cavity; dashed line: voltage for improperly functioning cavity with corresponding power generator off. Left figures, cavity is not detuned; right figures, cavity is detuned by 5 bandwidths. Top figures, $\delta = 0.1/Q$; bottom figures, $\delta = 1/Q$.

small,

$$\delta \leq \frac{1}{10Q}, \tag{6.1}$$

to have a possibility to bypass cavities not functioning properly. Figure 6.7 demonstrates the effects of cavity coupling and detuning on the cavity voltage. For a loaded Q of 5×10^5, the required cavity decoupling should be below 2×10^{-6}.

Such decoupling requires significant distances between nearby cavities. For an estimate, we take the coupling between cavity cells to be 5%, and then, using results presented

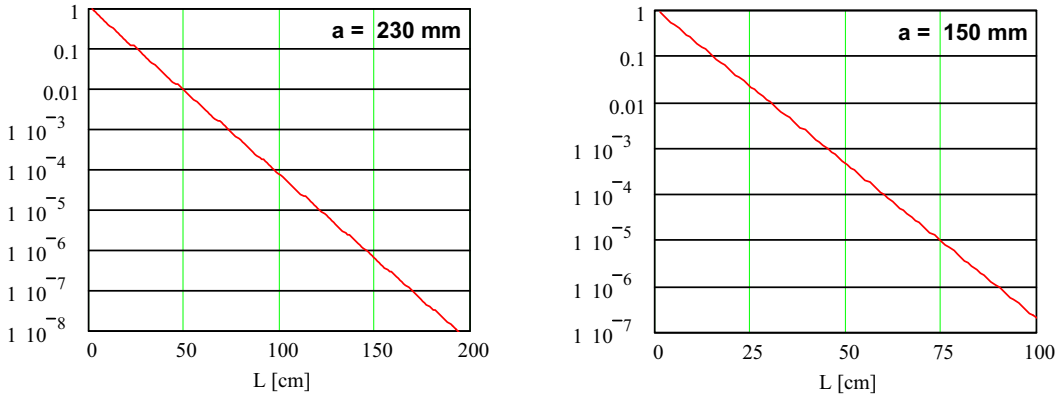

Figure 6.8: Attenuation of electromagnetic waves between two cavities for short (left) and long (right) cryomodules. The attenuation is approximated by $\delta = \exp(-L\sqrt{(\mu_0/a)^2 - (2\pi/\lambda)^2})$.

in Figure 6.8, find that the distance between cavities has to be more than 110 cm for short cryomodules and 70 cm for long cryomodules. Taking into account that the fundamental and HOM couplers are located in the same space, these distances were increased to 150 and 100 cm, respectively. BPMs are located inside the solenoids to reduce effects of EMI coming from the rf cavities.

There is an additional limitation on the layout of the linac determined by a requirement that all cavities be treated and placed under vacuum in a clean room and then kept under vacuum thereafter. To accomplish this, each cryomodule must have vacuum valves at both ends, with corresponding transition modules from liquid-helium temperature to room temperature. To achieve the maximum real-estate accelerating gradient, the focusing solenoids are also located inside the rf cryomodules.

Considering the large aperture required by the beam size, the question of focusing linearity of the solenoids must be addressed. The dependence of focusing strength on radius can be approximated by the following expression:

$$\Phi \equiv \frac{1}{F} \approx \left(\frac{e}{2pc}\right)^2 \left(\int B^2 ds + \frac{r^2}{2}\int B'^2 ds\right) \approx L\left(\frac{eB_0}{2pc}\right)^2 \left(1 + \frac{r^2}{3aL}\right), \qquad (6.2)$$

where L and a are the solenoid length and radius. As can seen from Eq. 6.2, to reduce the nonlinearity one needs to increase the solenoid length and aperture. Increasing length directly decreases the real-estate gradient; increasing the aperture requires a larger distance between the solenoid and cavity to shield the magnetic field and, in the final analysis, also decreases real-estate gradient. An aperture increase also makes solenoids

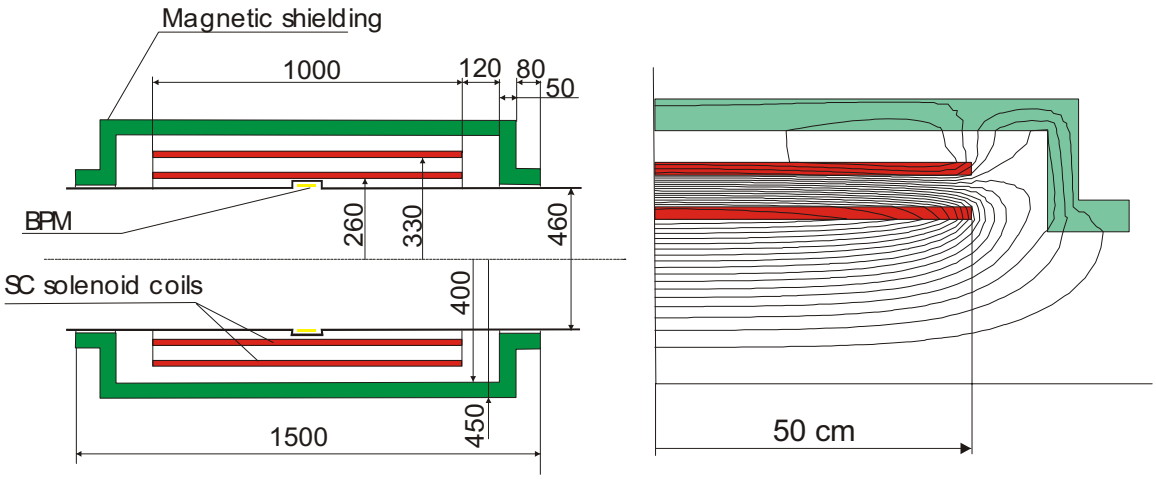

Figure 6.9: Layout of short solenoid and plot of its magnetic field lines.

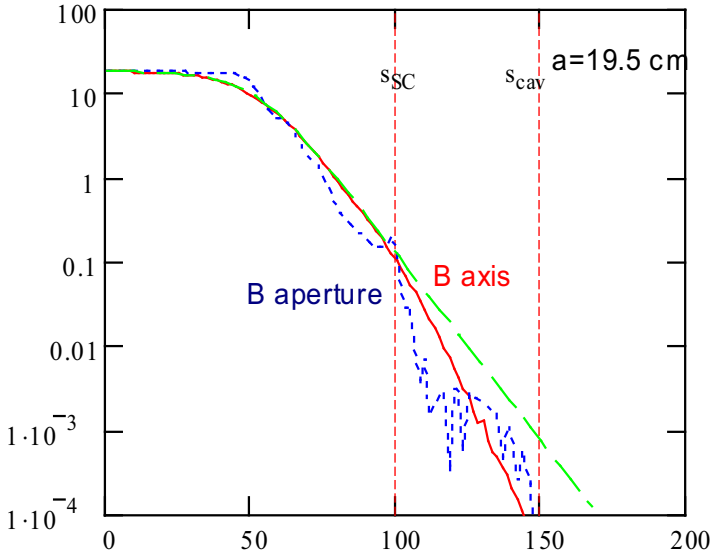

Figure 6.10: Dependence of magnetic field on longitudinal coordinate. The solid line is the field on axis; the dotted line is the field at the cavity radius (23 cm); the dashed line is a fit to $B(s) = (B_0/2)\{1 - \tanh[(s - L/2)/a]\}$, where $a = 19.5$ cm. Vertical lines show positions where the SC screen and cavity start.

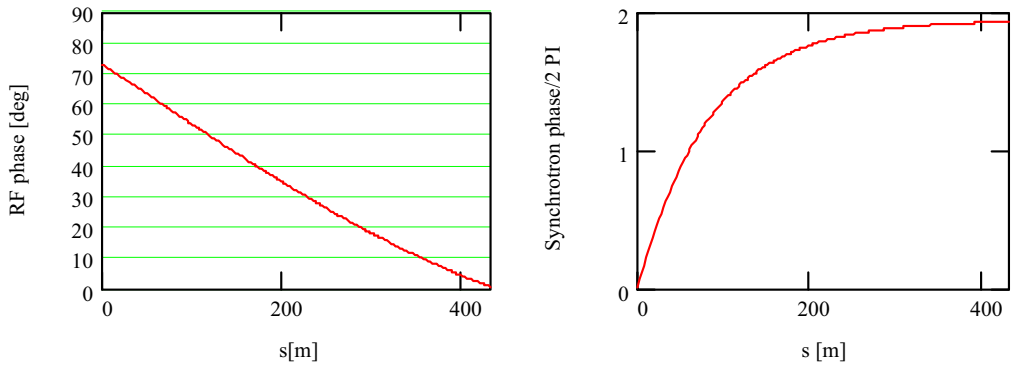

Figure 6.11: RF (left) and synchrotron (right) phases along the linac.

more expensive and less reliable. The length of the short solenoid has been chosen to be 1 m, as a compromise between these conflicting requirements. The length of the long solenoids is determined by the magnetic field limitation and is chosen to be 1.5 m. The concept of the short solenoid and plots of magnetic lines are shown in Fig. 6.9. Design details are given in Chapter 10. To achieve fast field drop between the solenoid and the cavity, the solenoid has an outer bucking coil that cancels its magnetic flux. It also has a SC shield at its outer surface. Together, these give a magnetic field less than 0.1 G inside the cavity, as depicted in Fig. 6.10.

6.1.3 Longitudinal Beam Dynamics

Because the initial bunch length and energy spread are very large, the bunch length is more than a half rf wavelength ($\Delta\phi = \pm 89°$), and the momentum spread is about $\pm 21\%$. Decreasing these values (via adiabatic damping) to a manageable level is the most important assignment of the beam acceleration in the linac. The final linac energy is determined by demanding a velocity sufficiently close to the velocity of light that there is no significant rf phase slip for higher passes in the subsequent recirculator.

To perform adiabatic bunching, the rf phase of the cavities is shifted by 73° at the beginning of the linac and is gradually changed to zero at the end of the linac, as shown in Figure 6.11. In the first half of the linac, when the beam is still not sufficiently relativistic, the offset results in synchrotron motion, which prevents a sag in acceleration for the bunch head and tail, and allows bunch compression in both length and momentum spread to $\Delta p/p = \pm 7.5\%$ and $\Delta\phi = \pm 23°$. However, the rf phase offset also reduces the effective accelerating gradient, so that a total voltage of 2.87 GV is required to provide a beam acceleration of 2.35 GeV. To maximize longitudinal acceptance, the initial position of the

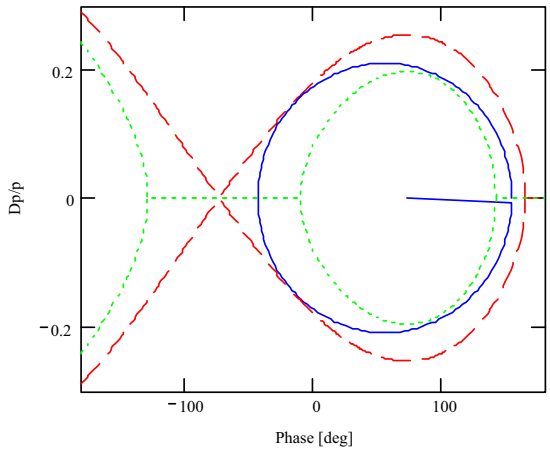

Figure 6.12: Beam boundary (solid line) inside separatrix (dashed line) shown at the beginning of the linac.

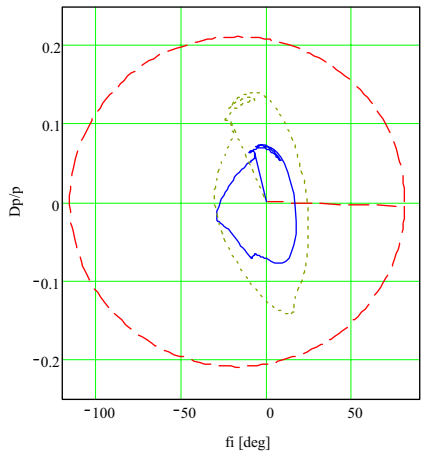

Figure 6.13: Beam boundary at the beginning (dashed line), in the middle (dotted line), and at the end of the linac.

beam is shifted relative to the center of the bucket. Figure 6.12 depicts the position of the beam boundary inside the separatrix; Figure 6.13 shows how the initially elliptical boundary of the bunch longitudinal phase space is transformed to the end of the linac.

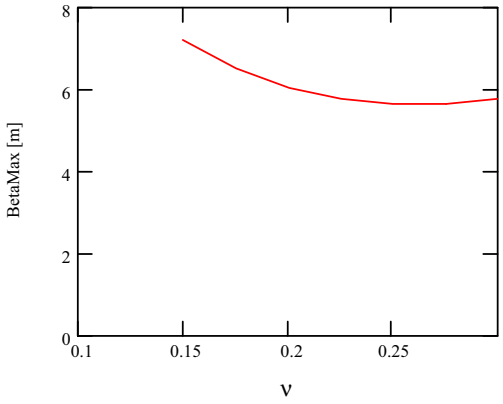

Figure 6.14: Dependence of maximum beta function on phase advance per cell for a beam line with solenoidal focusing and period length 6 m.

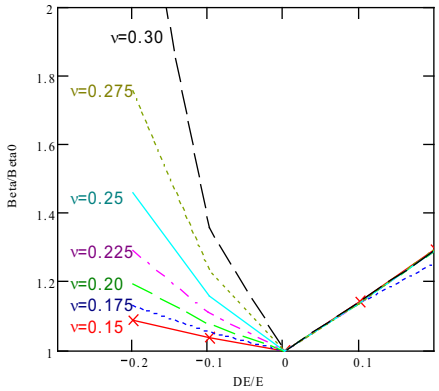

Figure 6.15: Dependence of relative change of the maximum beta function on the relative momentum change for different values of the phase advance per cell.

6.1.4 Transverse Beam Dynamics and Tracking

Betatron phase advance per cell, ν, is an important parameter to determine the properties of the beam transport in the linac. There are a few considerations that must be taken into account. First, large beam emittance and limited aperture in the cavities require minimization of the beam size for a given period length. As seen from Fig. 6.14, this requires ν close to 0.25. Second, we must minimize the dependence of the beta function

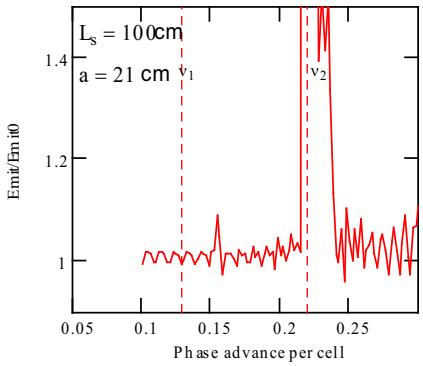

Figure 6.16: Relative emittance change after passing 50 solenoidal lenses of 1 m length. $\varepsilon_n = 15$ mm-rad; vertical lines show betatron tune spread in the beam: $\Delta\nu/\nu \approx \Delta p/p = \pm 26\%$.

on momentum. For the same initial conditions, the beta function oscillates relative to its nominal value if the momentum is changed. Figure 6.15 shows the ratio of maximum beta function achieved in the course of oscillations to the maximum beta function at equilibrium energy. For a momentum spread of $\pm 20\%$ a phase advance below 0.25 is clearly preferred. Third, the solenoids are short compared with their aperture, and therefore they have significant non-linearity in their focusing. From Eq. (6.2), for $a = 19$ cm, $r = 23$ cm and $L = 1$ m, there is a change of focusing strength of 9% at the beam boundary. Such nonlinear fields can cause strong nonlinear resonances, even for a small number of lattice periods. Figure 6.16 shows how the beam emittance changes for different values of the phase advance per cell after traversing a channel with 50 solenoidal lenses. One can see the very strong effect of the 1/4-resonance, which spreads over the 0.21–0.24 tune range. The 1/6-resonance is also visible, but does not produce so large an effect. In reality, this effect would be much smaller, because of adiabatic damping of the beam size with acceleration. Taking everything into account, we choose a phase advance of 0.175.

The particle distribution for tracking has been chosen to be Gaussian in 6D phase space, but the tails of the distribution are truncated at 2.5 σ, corresponding to the beam acceptance presented in Table 6.1. Despite the large initial energy spread, particle tracking through the linac does not exhibit any significant emittance growth, with 0.2% beam loss coming mainly from particles at the longitudinal phase space boundary. Figure 6.17 presents longitudinal phase space at the beginning and the end of the accelerator. Figure 6.18 shows the beam emittance, beam envelope, and beam intensity along the linac. The sudden increases and then decreases of the envelopes correspond to a particle motion instability, with subsequent particle scraping. The decay of muons is not taken into

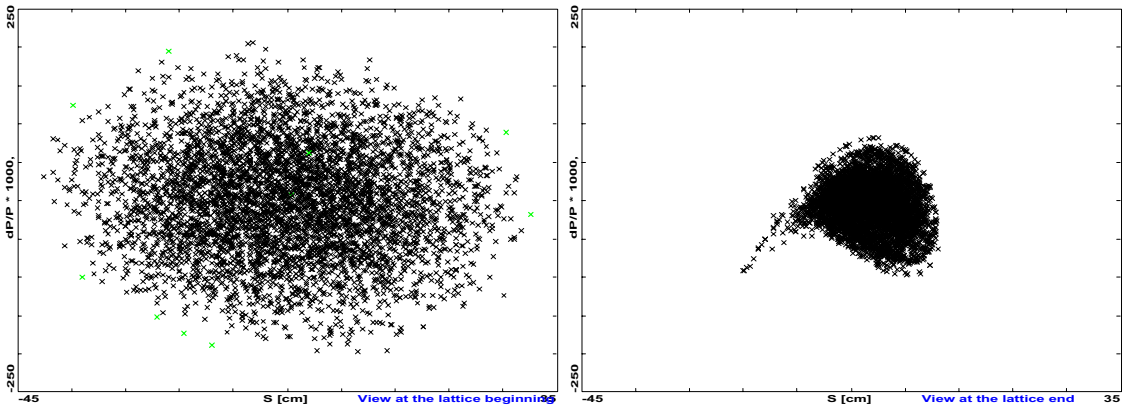

Figure 6.17: Longitudinal phase space at the beginning (left) and the end (right) of the linac.

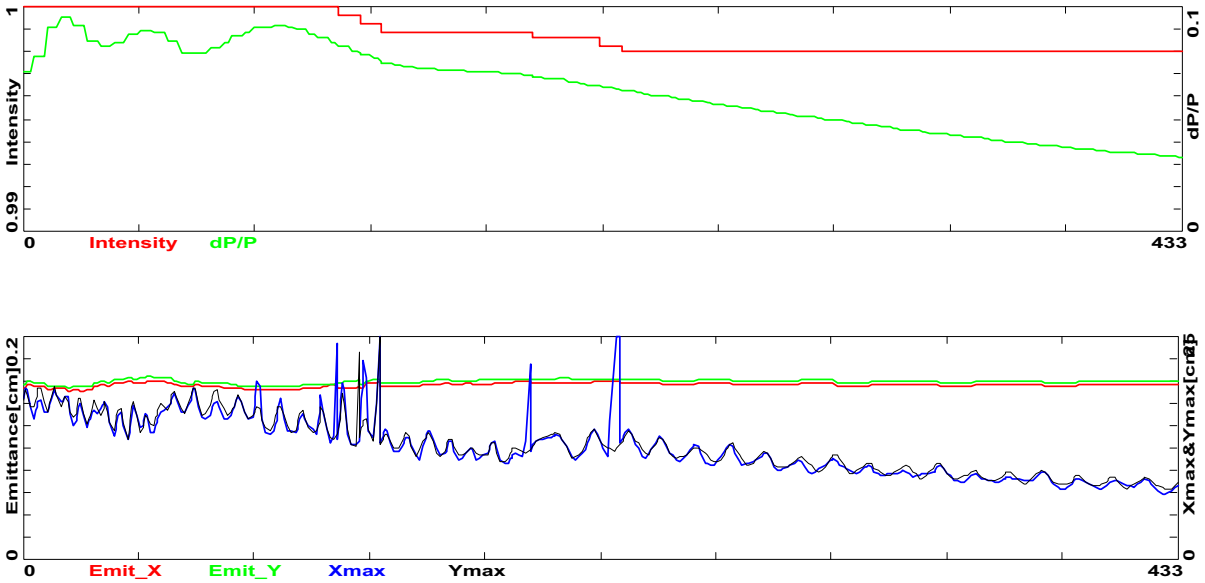

Figure 6.18: Beam intensity, rms momentum spread (top), beam emittances (normalized to the initial linac energy) and beam envelopes (bottom) along the linac.

account in this beam intensity plot.

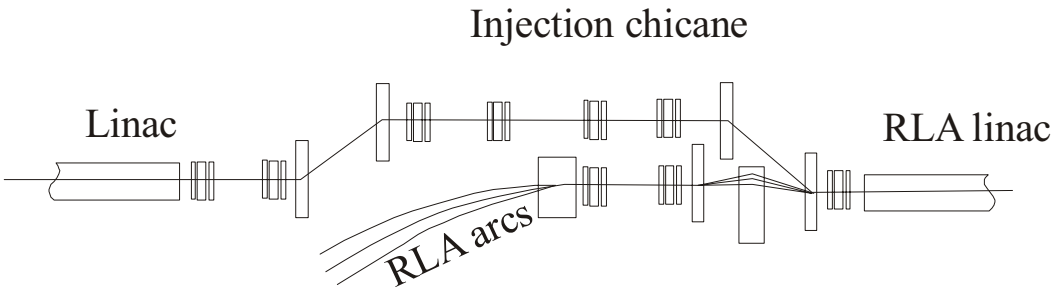

Figure 6.19: Diagram of the injection chicane.

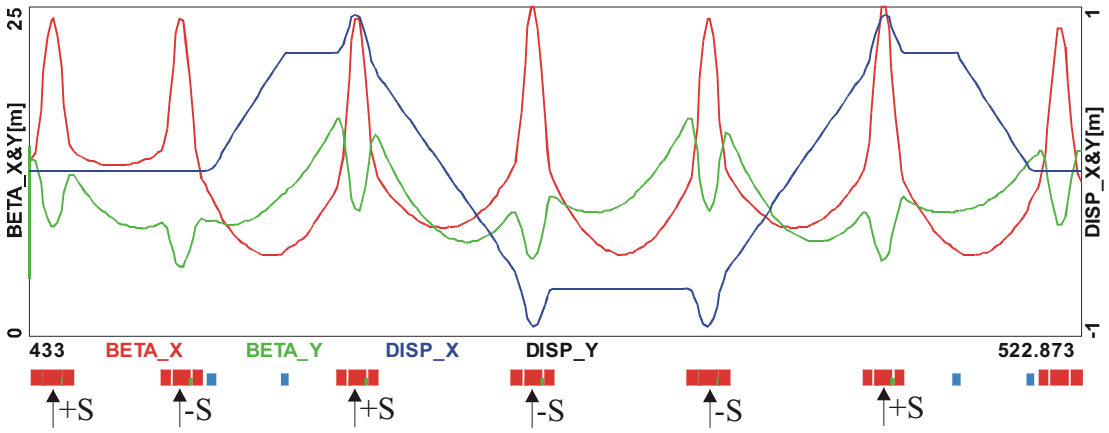

Figure 6.20: Beta functions and dispersion in the injection chicane.

6.1.5 Injection Chicane

An injection chicane is used to inject the beam into the RLA. A simplified scheme is presented in Figure 6.19. The chicane is built from four dipoles with four quadrupole triplets between them to form an achromat. A standard three-dipole chicane cannot be used because the chicane has to be sufficiently long to bypass the incoming higher energy arcs. In addition, two quadrupole triplets are used immediately before the chicane in place of the solenoidal focusing in the linac. An advantage of triplet focusing is that it easily provides the long straight sections necessary for beam separation at injection. Triplet focusing also naturally matches the solenoidal focusing. The period length is 15 m to coincide with the period length of the downstream RLA linac. The betatron phase advance per cell is chosen to be 90°, as this is preferable from the viewpoint of compensating chromatic effects. Figures 6.20 and 6.21 depict beta functions, dispersion,

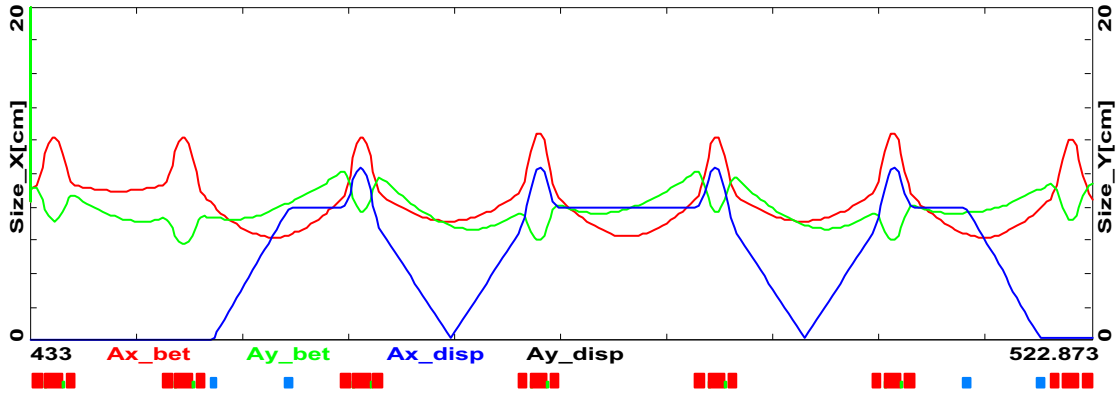

Figure 6.21: Beam envelopes in the injection chicane.

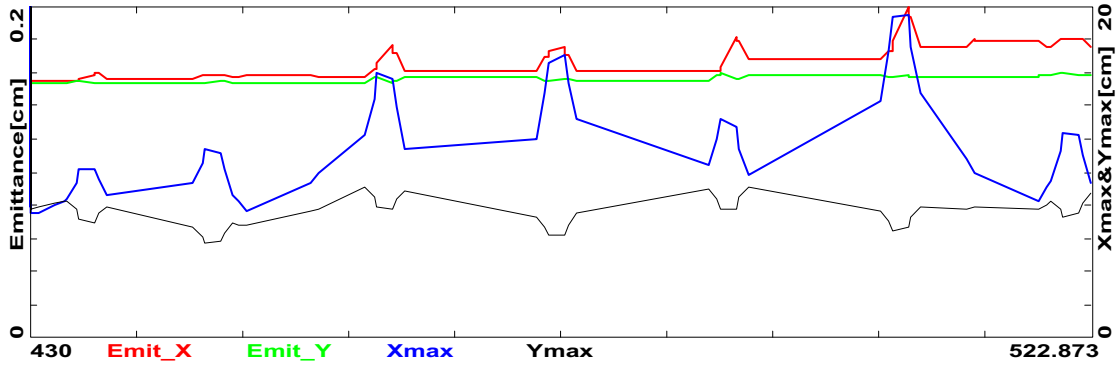

Figure 6.22: Variation of beam emittance (normalized to the initial linac energy) and beam envelopes along the linac.

and beam envelopes in the chicane.

In the linac, chromatic effects are suppressed by the periodicity of the focusing and do not require special correction. Unfortunately, it does not quite work the same way when we introduce bends; a sextupole chromatic corrector is required for the horizontal plane. This is achieved by introducing sextupole components into the field of the focusing quadrupoles of the six triplets. Four of these quadrupoles are located at the maximum of the dispersion function for chromaticity compensation and the other two are located in front of the chicane for compensation of the nonlinearity introduced by the strong chromaticity-correction quadrupoles, as shown in Fig. 6.20. Tracking studies showed that the nonlinearity of the sextupole fields can be cancelled for a small beam momentum spread, but only partial cancellation can be achieved for a momentum spread

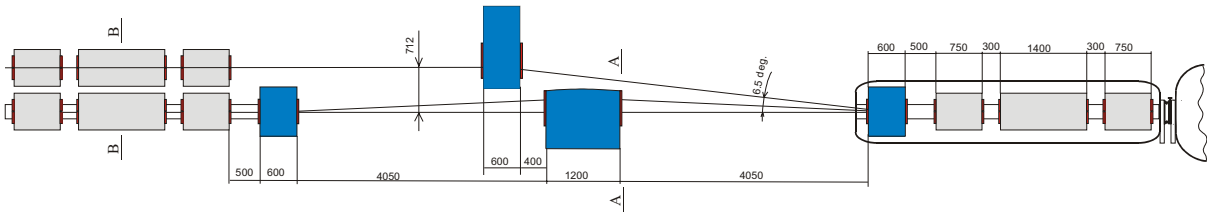

Figure 6.23: Layout of the injection chicane at the separation point.

Table 6.4: Parameters of the injection chicane quadrupoles.

	Number of magnets	Maximum gradient (T/m)	Length (m)	Aperture (m)	Built-in sextupole, S/G (m^{-1})
Focusing quad	3	4	1.40	0.15	0
Defocusing quad	14	4	0.75	0.15	0
Large aperture quad	4	4	1.40	0.181	0.355

as large as ±10%, the value at the end of the linac (see Fig. 6.17). Strong sextupole components, required for good correction of second-order dispersion, cause emittance growth that is too large, due to inadequate cancellation of nonlinearities, and therefore a partial compensation of second-order dispersion is preferable. In tracking studies, values of all six sextupole components were varied independently to minimize the overall emittance growth through the chicane. It was found that if all sextupole components are proportional to the corresponding quadrupole components (the preferable technical choice), the emittance growth is close to its minimum value. Such a choice required only one additional type of quadrupole, and therefore it was adopted. The optimal ratio of sextupole to quadrupole components is $S/G = 0.355$ m^{-1}, which corresponds to a 7% correction of quadrupole gradient at a radius of 20 cm. Figure 6.22 depicts the beam envelopes and the beam emittances normalized to the initial linac energy, $\varepsilon\gamma\beta/\gamma_0\beta_0$. The horizontal emittance grows by 13% and the vertical by 3%, with no losses. Maximum horizontal beam size occurs at the last chicane triplet and is equal to ±19 cm.

Figure 6.23 shows the injection chicane in the vicinity of the separation point. To minimize emittance growth, the bend angles of the chicane dipoles are chosen to be as small as possible. The separation is determined by the beam sizes and the space required for the septum magnet coil. Figures 6.24 and 6.25 show cross sections of the injector chicane at the separation point and in the center of the focusing quad. Taking into account the large apertures of the magnets (about 30 cm) and their comparatively

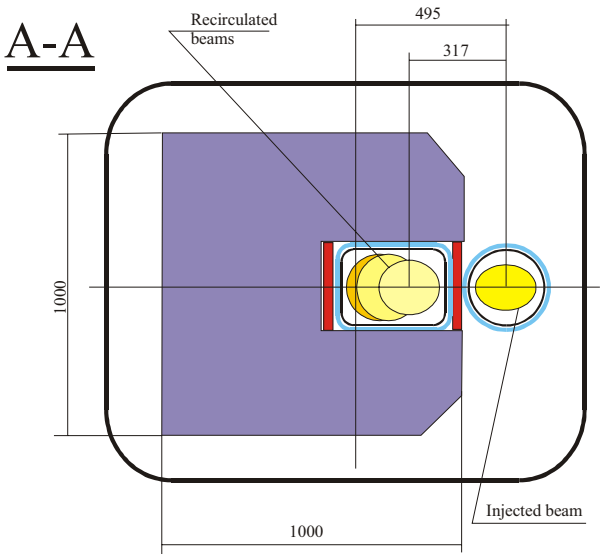

Figure 6.24: Cross section of the injection chicane at the separation point.

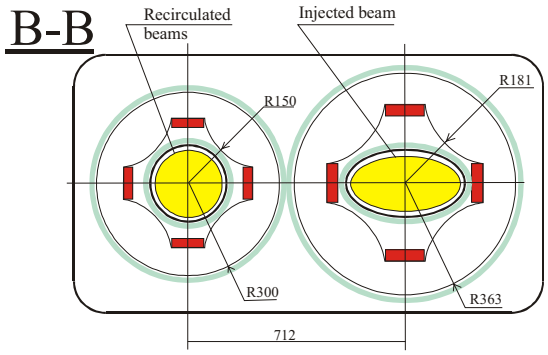

Figure 6.25: Cross section of the injection chicane at a focusing quadrupole.

modest magnetic fields (< 2 T), it looks preferable to use magnets with SC coils but with the field formed by the cold-iron core. Such a choice allows compact magnets and a significant reduction in required power. Tables 6.4 and 6.5 present parameters of dipoles and quadrupoles used for the injection chicane.

6.1.6 Solenoid Magnets

The linac contains several different solenoid magnets to provide focusing. The end of the matching section consists of a pair of low-stray-field solenoids with adjustable currents

Table 6.5: Parameters of injection dipoles.

	Number of magnets	Maximum field (T)	Length (m)	Gap (m)	Width (m)
Short dipole	4	1.7	0.6	0.30	0.30
Long septum	1	1.7	1.2	0.30	0.38
Short septum	1	1.7	0.6	0.30	0.38

for tuning. The short and intermediate modules have a 1-m focusing solenoid with a 1.25-m straight section at each end. Likewise, the long modules have a 1.5 m solenoid with a 1.25-m separation to the first rf cavity cell.

Unlike focusing quadrupoles, focusing solenoids produce a stray field that reaches far from the magnet. Superconducting rf cavities are sensitive to magnetic fields even at the gauss (10^{-4} T) level, so as noted in Section 6.1.2}, a key parameter in the superconducting focusing solenoid design is getting rid of the solenoid stray field in the rf cavities. The approaches one can use to eliminate the stray field in the rf cavities are described in Chapter 10.

6.2 Recirculating Linac (RLA)

6.2.1 Arc Optics, Spreaders, and Recombiners: Design Choices

For multiple practical reasons, horizontal rather than vertical beam separation was chosen. If vertical separation were chosen, one of the drawbacks would be an enormous vertical aperture of the vertical spreader/recombiner dipole. Furthermore, instead of having to suppress vertical dispersion created by the spreaders and recombiners we can use horizontal separation with no dispersion suppression; it is matched to the horizontal dispersion of the arc. Finally, to ensure a compact arc architecture, very short matching sections (three triplets) were implemented in the spreaders and recombiners.

The 4-pass RLA beam transport system uses a single dipole separation of beams at the end of each linac to allow independent recirculation of each pass. Individual recirculation arcs are based on a periodic triplet-focusing structure, which is a smooth continuation of the linac focusing. Betatron phase advance per cell is chosen to be 90°, which is preferable from the point of view of compensating chromatic effects. The period length (about 11 m) is slightly shorter than for the linacs, to achieve the desired small value of

M_{56} (about 1.4 m).

Triplet focusing has a few advantages over the FODO focusing structure. First of all, it has larger distance between quadrupoles, which significantly simplifies spreader/recombiner design. Spreading and recombining the beams with a FODO lattice would be much more complicated. Furthermore, triplet focusing allows simple and smooth beam envelope matching from linac to recirculating arc, which is very important for beams with such a large energy spread. Finally, triplet focusing has only half the chromaticity of the vertical beam envelope compared with FODO focusing, so it requires chromatic corrections in only one plane.

Another crucial beam transport issue is to maintain manageable beam sizes in the arcs. This calls for short cells and for putting stringent limits on dispersion and beta functions (beam envelope). Since spreaders and recombiners were chosen in the horizontal plane, the uniform focusing and lattice regularity is broken in that plane, and the horizontal beam envelope requires special attention. On the other hand, the vertical beam size remains small due to maintaining uniform focusing (unbroken periodic symmetry) and small beta functions in that plane.

Furthermore, there is a need for high periodicity and a smooth transition between different types of optics, *e.g.*, linac-arc-linac, to alleviate emittance dilution due to chromatic aberrations (second-order-dispersion).

Finally, the required large momentum acceptance necessitates introduction of a chromatic correction scheme using three sextupole families for the off-momentum orbit and path length. As in other recirculating linacs, and unlike storage rings and synchrotrons, correction of betatron "tunes" is unnecessary. Figure 6.26 shows a geometric layout of arcs 1, 3, 5 and 7.

6.2.2 Longitudinal Dynamics in Recirculating Linac

The beam bunch length and energy spread are still too large at the RLA input, and further compression is required in the course of the acceleration. To achieve this, the beam is accelerated off-crest with non-zero M_{56} (momentum compaction). This causes synchrotron motion, which suppresses the longitudinal emittance growth related to nonlinearity of the accelerating voltage. Without synchrotron motion, the minimum beam energy spread would be set by the nonlinearity of the rf voltage at a value of $(1 - \cos\phi) \approx 6\%$ for a bunch length of $\phi = 20°$.

Synchrotron motion causes particle motion within the bunch and equalizes the total average energy gain of particles in the tail and particles in the core. The parameters of acceleration are presented in Table 6.6, and corresponding boundaries of longitudinal

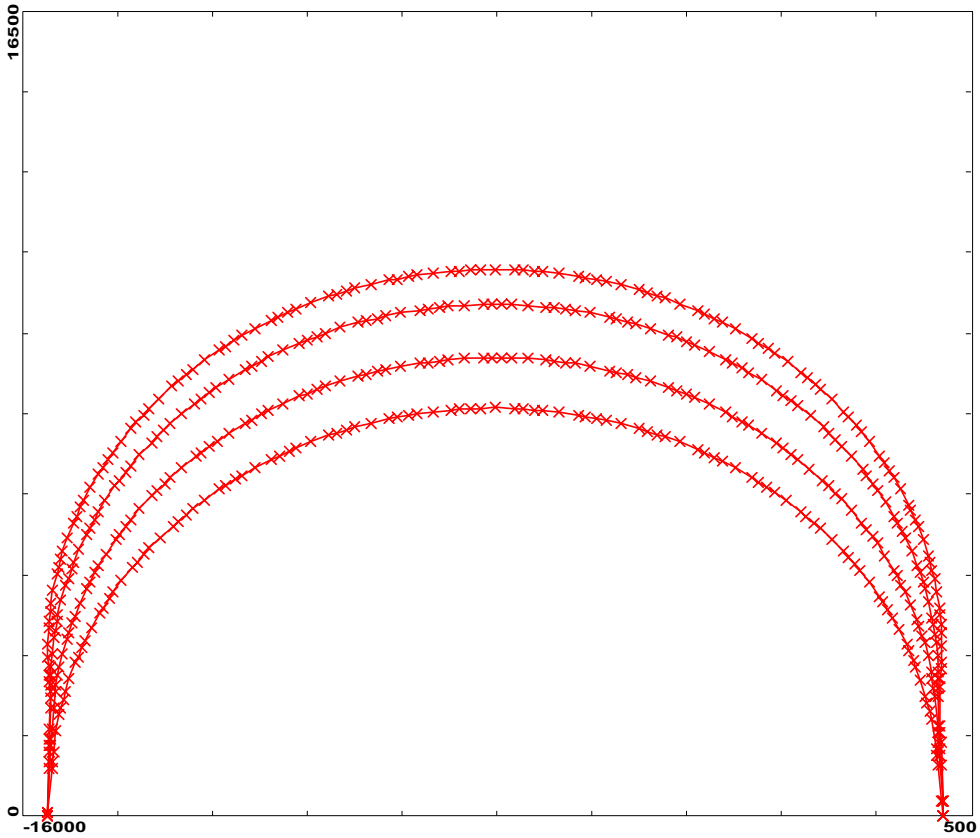

Figure 6.26: Geometric layout (bird's eye view) of odd numbered arcs, including spreader/recombiner configuration. Crosses mark locations of magnets (dipoles and quadrupoles). All distances are in cm.

phase space are presented in Figure 6.27. We chose to have approximately the same M_{56} for all the arcs; the optimum value is about 1.4 m. Optimal detuning of the rf phase from the on-crest position is different for different arcs. Although longitudinal motion is still quite nonlinear, it is possible to reduce the energy spread by a factor of 4.7, to $\pm 1.6\%$, with emittance dilution of about 75%. In these calculations for arc optics we assume that the longitudinal displacement is a function of momentum only, given by the linear function, $\Delta L/L = M_{56}\Delta p/p$. The horizontal and vertical acceptances of the arcs listed in Table 6.6 are presented with emittance dilutions of 9% to 4% per arc. This is supported by preliminary tracking results. Final details of the beam dynamics depend on the beam transport optics and can be determined only by tracking (discussed below).

Table 6.6: Parameters for acceleration in the recirculator.

	Kinetic energy (GeV)	Gang phase (deg)	Total energy spread, $2\Delta p/p$ (%)	Horizontal acceptance (mm-mrad)	Vertical acceptance (mm-mrad)
Entrance	2.480	0	15.0	669	638
Arc 1	4.756	-23	11.3	384	350
Arc 2	6.884	-23	8.9	292	253
Arc 3	9.017	-23	6.7	244	202
Arc 4	11.140	-23	5.8	216	171
Arc 5	13.284	-20	5.0	198	150
Arc 6	15.462	-16	4.4	187	134
Arc 7	17.690	-5	3.4	178	122
Exit	20.000		3.2	157	108

Since the beam intensity is high, beam loading has to be taken into account. It causes the rf voltage to droop by about 0.6% per pass, yielding about 2.4% loss in acceleration for the tail bunch of the last pass. This is comparable with the energy aperture of the later arcs and their optics tuning must be done with energy droop taken into account. In this scenario, the first and the last bunches see different accelerating voltage and experience different longitudinal dynamics. Fortunately, accelerating off-crest resolves this issue as well. In this case, after acceleration in the first linac, the last bunch experiences less acceleration; but then, because of smaller energy, the bunch comes faster through the first arc and is accelerated with smaller rf phase, causing higher acceleration, in the next linac. In other words, the bunch center of the last bunch experiences synchrotron motion relative to the center of the first bunch. This suppresses the effect of accelerating voltage droop. Figure 6.28 shows the longitudinal phase space for the first and the last bunches at the end of the accelerator. The acceleration has been optimized so that the energy spread of both bunches is the same. Although the beam loading significantly changes the bunch shape, the energy droop cannot be seen.

6.2.3 General Parameters and Period Layout of RLA Linac

Both RLA linacs have the same period. One period comprises a cryomodule with four SC cavities and a cryomodule with a quadrupole triplet; the layout is presented in Figure 6.29. The design and parameters of the cavities are the same as for the cavities of the long cryomodule of the preaccelerator linac (see Table 6.3). However, in contrast to

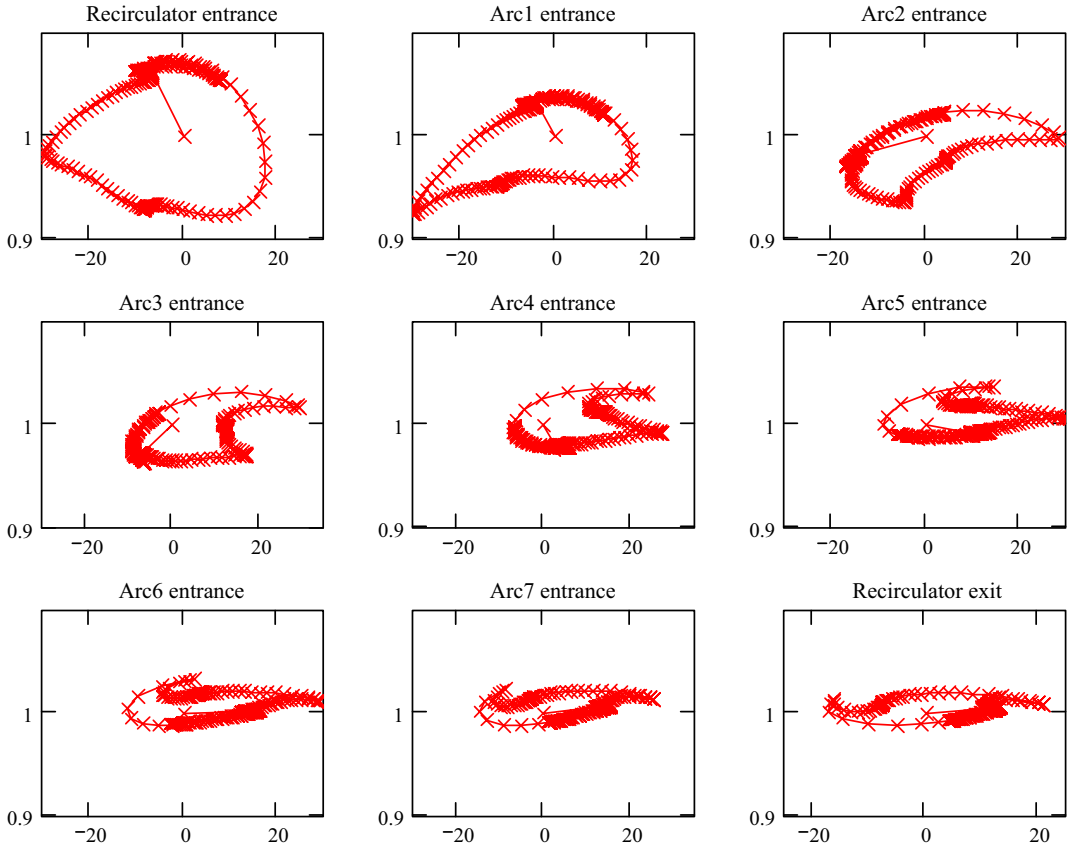

Figure 6.27: Boundaries of the beam longitudinal phase space at different locations in the recirculator; $M_{56} = 1.4$ m.

the preaccelerator linac, which has just one cryomodule per period, the RLA period has separate cryomodules for cavities and for magnets. This solution is preferred due to the increased length of the RLA period. The design and parameters of the triplets of the first RLA linac are similar to those of the small triplets of the injection chicane, but with higher focusing gradients ranging from 3.2 – 6.7 T/m. Quadrupoles of the second RLA linac have a similar design but with 1.5 times smaller aperture (100 mm). Their focusing gradient ranges from 6.2 – 9.7 T/m.

Figures 6.30–6.33 show the beta-functions and beam envelopes for the first and the last passes in the first RLA linac. Beta functions of the first pass in the second RLA linac are the same as for the first RLA linac. The last pass beta functions of the second RLA linac are smaller than the corresponding beta functions of the first RLA linac because

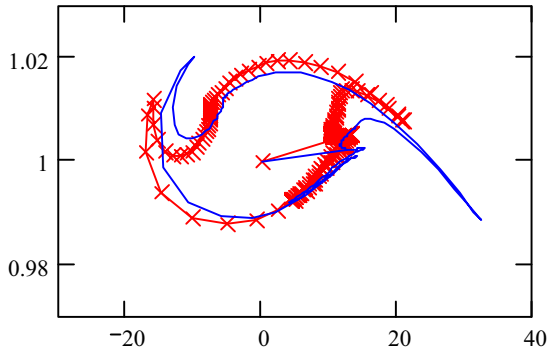

Figure 6.28: Boundaries of the beam longitudinal phase space at the end of the recirculator for the first bunch (line with crosses) and the last bunch (solid line). $M_{56} = 1.4$ m; the energy droop of 0.5% per pass corresponds to 3×10^{12} muons in the bunch train.

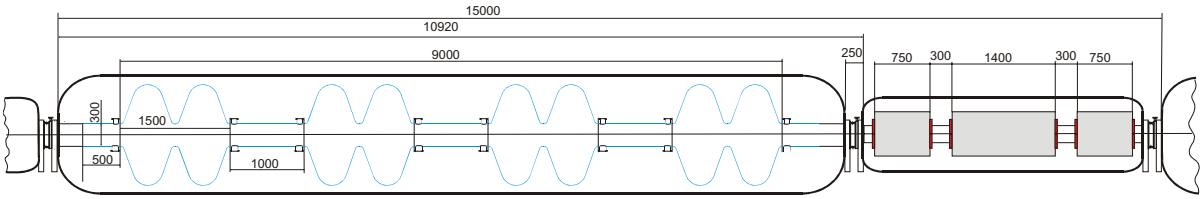

Figure 6.29: Layout of an RLA linac period.

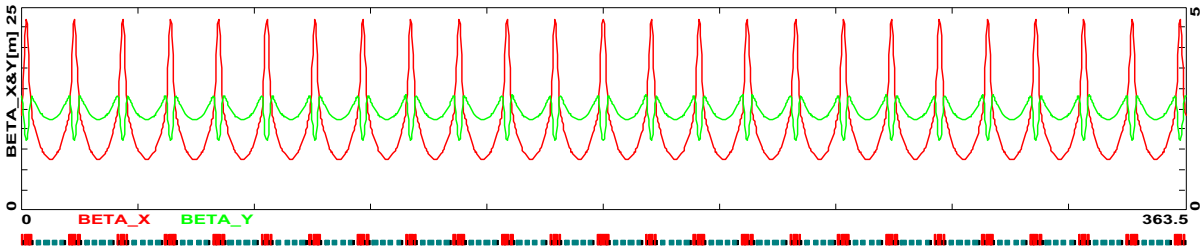

Figure 6.30: Beta functions for the first pass of the first RLA linac.

of a smaller energy difference between the last and the first passes. Figures 6.34 and 6.35 show the beam envelopes for the first and the last passes in the second RLA linac. The difference between the vertical and horizontal beam sizes for the last pass is related to a larger horizontal emittance resulting from higher horizontal emittance growth. The focusing structure for both linacs is chosen to give the same betatron phase advance per cell for the first-pass beam. The requirement to have similar horizontal and vertical beta

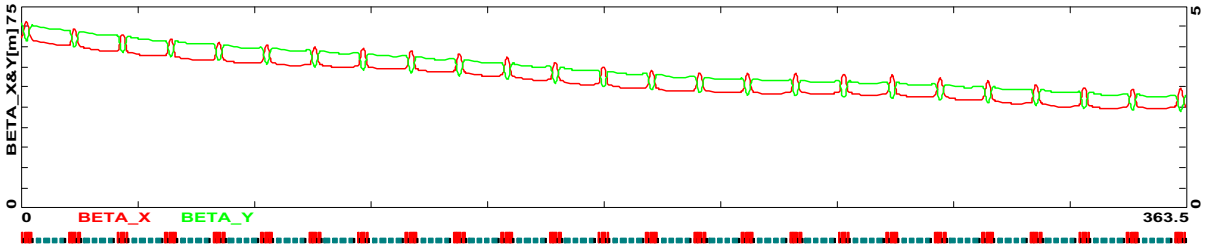

Figure 6.31: Beta functions for the last pass of the first RLA linac.

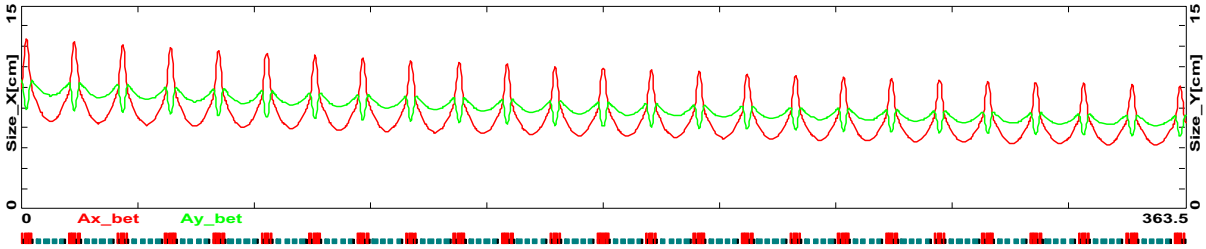

Figure 6.32: Beam envelopes for the first pass of the first RLA linac.

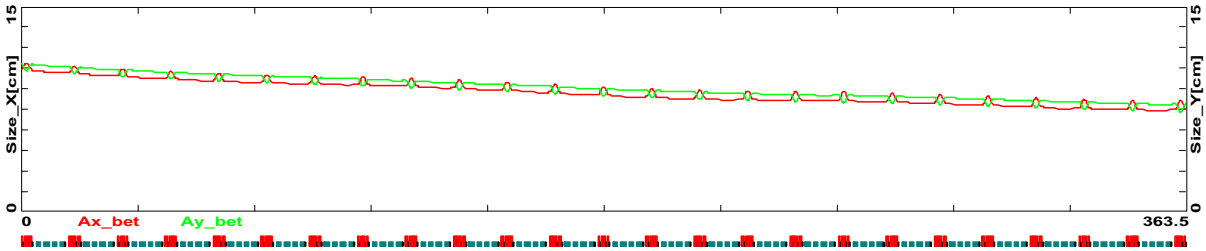

Figure 6.33: Beam envelopes for the last pass of the first RLA linac.

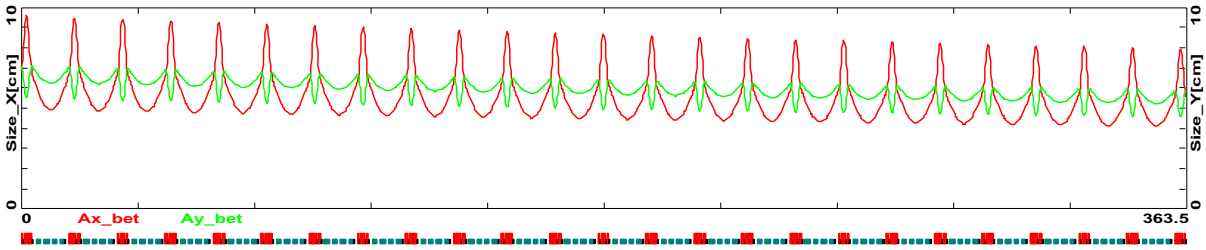

Figure 6.34: Beam envelopes for the first pass of the second RLA linac.

functions for the higher passes determines that the horizontal and vertical phase advances are not equal. Figure 6.36 shows the line on the tune diagram where the horizontal and

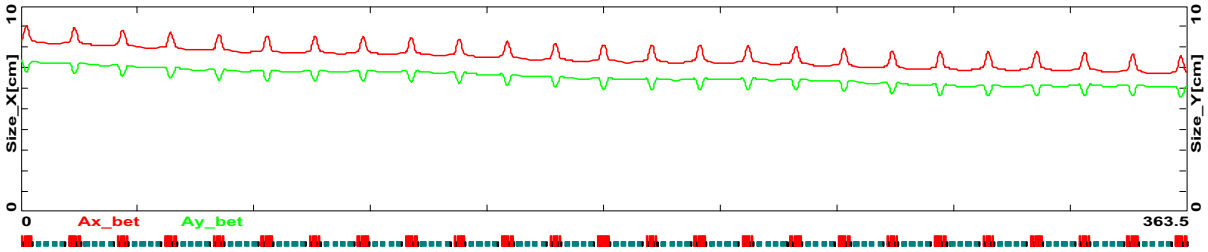

Figure 6.35: Beam envelopes for the last pass of the second RLA linac.

Table 6.7: Parameters of the RLA linac periods.

	Linac 1	Linac 2
No. of periods	24	24
Total length of one period (m)	15	15
No. of cavities per period	4	4
No. of cells per cavity	2	2
No. of couplers per cavity	2	2
Cavity accelerating gradient (MV/m)	17	17
Aperture in cavities, $2a$ (mm)	300	300
Aperture of quadrupole, $2a$ (mm)	300	200
Focusing quad length (m)	1.4	1.4
Defocusing quad length (m)	0.75	0.75
Quadrupole gradient (T/m)	3.2–6.7	6.2–9.7

vertical beta functions are approximately equal for the last pass of the first RLA linac. Parameters of linac periods are presented in Table 6.7.

Each cavity cryomodule has vacuum valves at both ends and is delivered to the tunnel under vacuum. These valves are slow; it is not feasible to build a sufficiently fast valve to prevent a major vacuum failure in a chamber of so large an aperture. Therefore each linac is separated from the arcs with 0.5-mm beryllium windows. This approach also resolves the question of differential pumping between the high vacuum in the RLA linacs and the low vacuum in the arcs, which otherwise would be a major issue with a vacuum chamber of such large aperture. The design and size of the windows are similar to the beryllium windows used for the ionization cooling. Altogether there are 5 windows: one in the injection chicane, and one at each end of both RLA linacs. Multiple scattering causes the total emittance growth of about 5% for windows of 0.5-mm thickness. The contribution to emittance growth from different passages through the windows is almost even: the

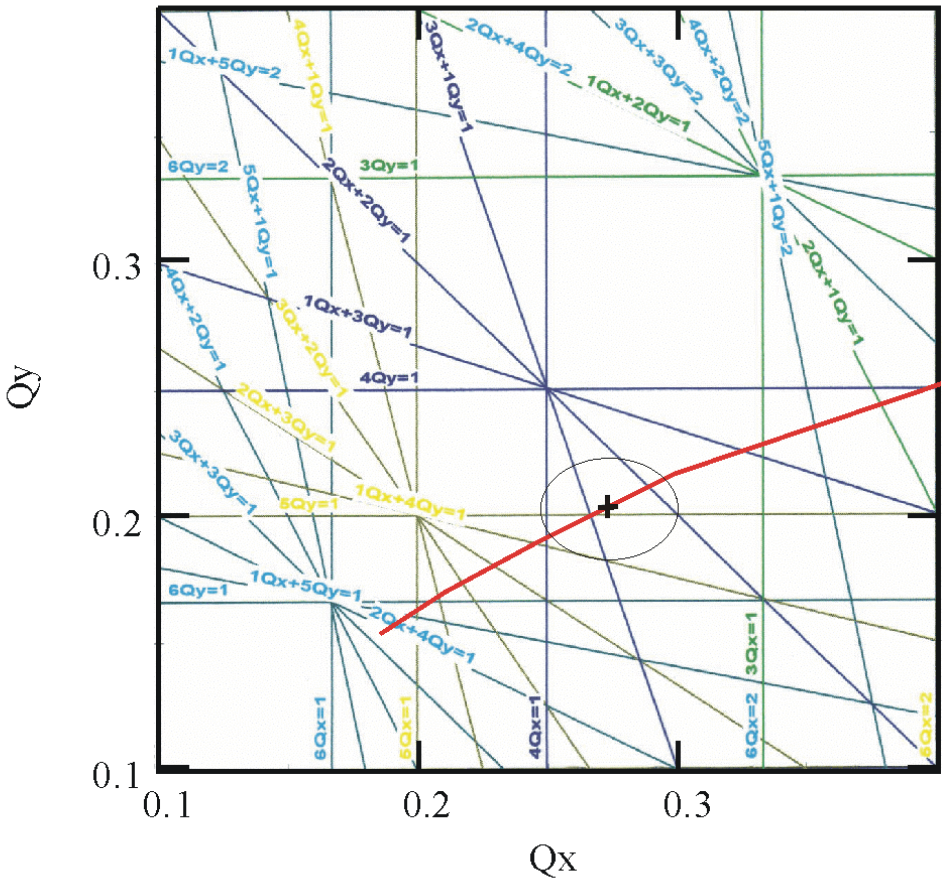

Figure 6.36: Tune diagram for one period of the first pass in the RLA linac. Solid line shows tunes where $\beta_x = \beta_y$ for the highest energy pass. The cross shows the chosen tune, $Q_x = 0.273$, $Q_y = 0.204$, and the circle around it corresponds to the tune changes corresponding to 10% energy spread.

beam of higher energy experiences smaller scattering, but it has a proportionately larger beta function in the RLA.

6.2.4 Beam Dynamics in the RLA Linacs

To choose a working point we took into account the following considerations. First, due to the symmetry of the quadrupole field, the lowest nonlinearity of its field has sixth-order

Table 6.8: Acceptable nonlinear fields of quadrupoles.

	4th order (octupole)	6th order	8th order
$\lvert F_n \rvert$	< 0.015	< 0.02	< 0.02

symmetry, so we would like to avoid sixth-order resonances. Second, the beam size should be close to its minimum for a given period length. Third, the chromaticity of the beam envelopes should be minimized. The chosen tunes of $Q_x = 0.273$, $Q_y = 0.204$ satisfy the above requirements. For higher passes, the phase advance per cell is not constant and grows from the beginning to the end of the linac, causing the tune to cross a few resonances. The most sensitive is the second pass, during which tunes cross the sixth-order resonances. Nevertheless, the tracking showed that all higher passes are less sensitive to quadrupole nonlinearity than the first pass. The first RLA linac is more sensitive to quadrupole nonlinearity because it has larger beam size for all passes. Therefore, it sets the limit for acceptable quadrupole nonlinearity. For simulations we assumed that nonlinear terms are proportional to the quadrupole gradients. The nonlinearity is described by the parameter

$$F_n = \frac{1}{Ga}\frac{a^{n-1}B_n}{n!}, \tag{6.3}$$

which determines a relative correction of the gradient at the reference radius a. Table 6.8 summarizes results of simulations performed for the first RLA linac. The values correspond to a reference radius of 10 cm, which is close to the beam envelope in the focusing quadrupoles. We find that the requirements for quadrupole nonlinearity are very modest and should be easily met. Summarizing, we can conclude that an accuracy of the quadrupole field integral better than 1% at the reference aperture of 100 mm is sufficient. With this assumption, tracking in the linacs did not exhibit any significant emittance growth, demonstrating that the periodicity of motion is not badly broken in the arcs.

As was already mentioned, there is a significant rf phase slip for the beam during different passes because of different particle velocities at different energies. Figure 6.37 presents rf phases for the beam at different passes, assuming that the cavity phases are set so that the second-pass beam is on crest. We see that the first-pass beam in the first RLA linac has phase variations in the range of about -19 to 12°. This reduces the effective accelerating gradient by 1.2%, but it does not otherwise produce any significant effect for higher passes.

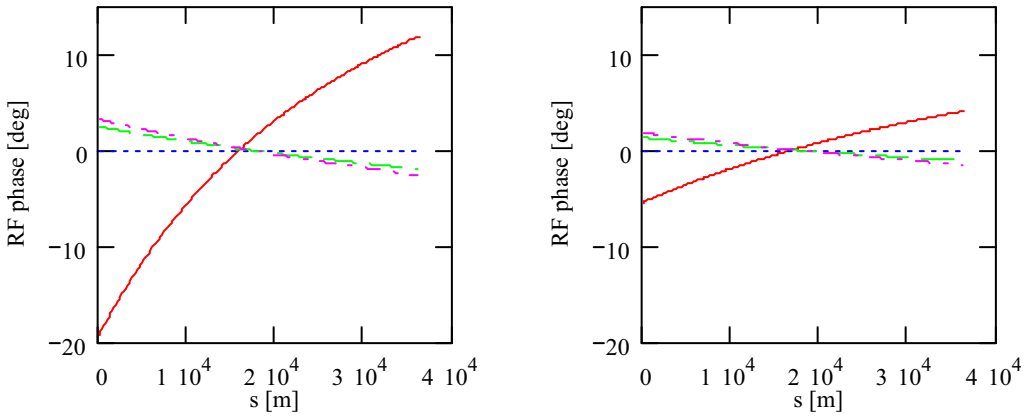

Figure 6.37: RF phase for different passes through the first (left) and second (right) RLA linacs. The solid line is pass 1, the dotted line is pass 2, the dashed line is pass 3, and the dot-dashed line is pass 4.

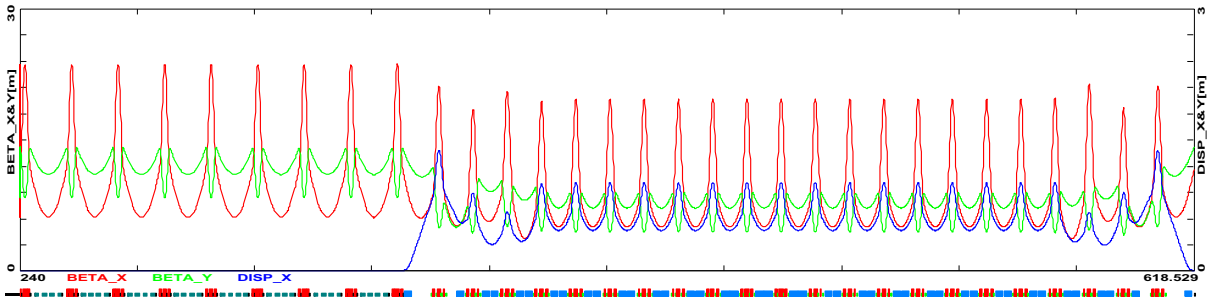

Figure 6.38: Arc 1 optics. Beta functions and the horizontal dispersion for the end of linac 1 and arc 1 (matched to both adjacent linacs).

6.2.5 Odd Arcs: Proof-of-principle Lattice Design

Lattices for four odd arcs and one even arc of the RLA are illustrated in terms of the beta functions and dispersion in Figs. 6.38–6.42. Short matching sections in spreaders and recombiners (consisting of six quadrupoles) allow us to match all Twiss functions and to smoothly join regions of different optics of the adjacent linacs.

The number of periodic cells in the arc was chosen and tuned so that the desired value of momentum compaction factor required for optimum longitudinal phase space compression ($M_{56} = 1.4$ m) is built into the arc optics.

Similar optics for one full turn in the RLA (linac1-Arc1-linac2-Arc2), as illustrated in Figures 6.38 and 6.39, was put to the test for beam transport properties in Study I. A

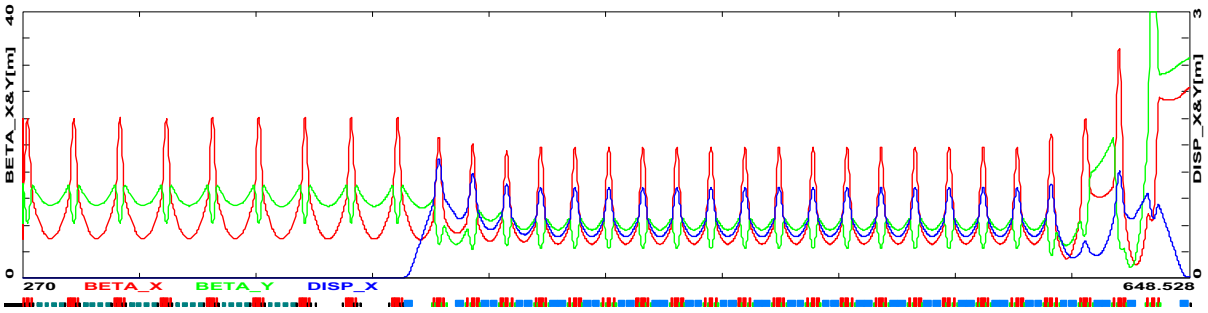

Figure 6.39: Arc 2 optics. Beta functions and the horizontal dispersion for the end of linac 2 and arc 2 (matched to both adjacent linacs).

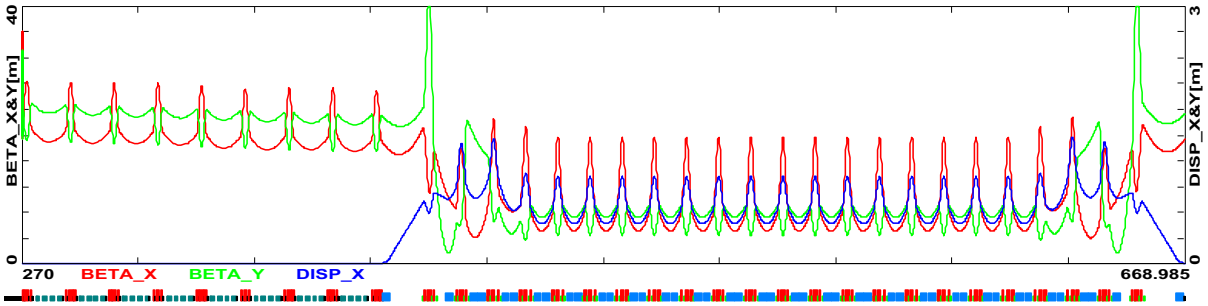

Figure 6.40: Arc 3 optics. Beta functions and the horizontal dispersion for the end of linac 3 and arc 3 (matched to both adjacent linacs).

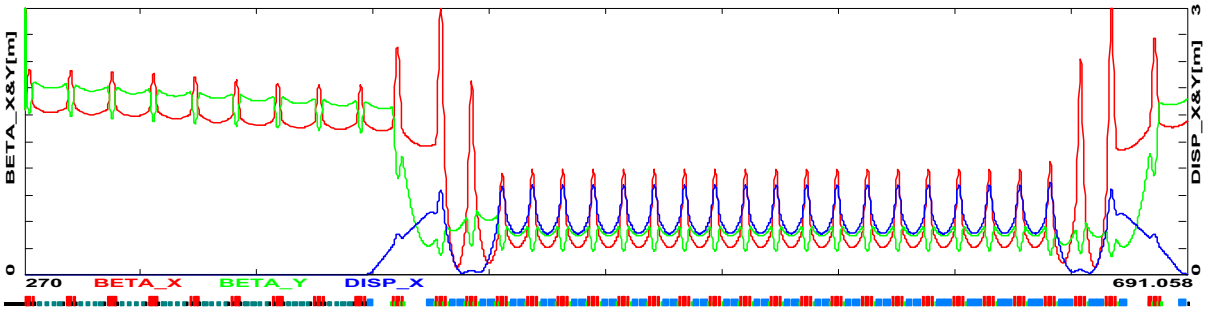

Figure 6.41: Arc 5 optics. Beta functions and the horizontal dispersion for the end of linac 5 and arc 5 (matched to both adjacent linacs).

multi-particle simulation was carried out for a particle distribution having a realistic large momentum spread (10%). The particle distribution used for tracking was Gaussian in 6D phase space with the tails of the distribution truncated at 2.5σ, corresponding to the

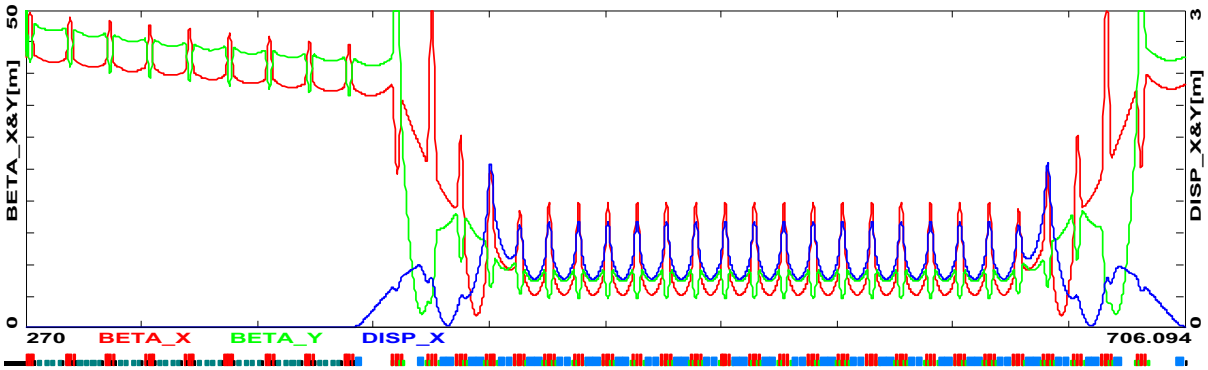

Figure 6.42: Arc 7 optics. Beta functions and the horizontal dispersion for the end of linac 7 and arc 7 (matched to both adjacent linacs).

beam acceptance presented in Table 6.6. Despite the large initial energy spread, particle tracking through the linac does not exhibit any significant emittance growth. There was less than 0.5% beam loss, coming mainly from particles at the longitudinal phase space boundary. The simulation also showed that the chromatic corrections via three families of sextupoles in the spreaders/recombiners are a very effective means of emittance dilution control.